All-printed smart label with integrated humidity sensors and power supply

Nelson Pereira, Vitor Correia, Nikola Peřinka, Carlos M. Costa and Senentxu Lanceros-Méndez**

N. Pereira and Dr. C. M. Costa
Centro de Física, Universidade do Minho, 4710-057 Braga, Portugal
E-mail: cmscosta@fisica.uminho.pt

N. Pereira and Dr. V. Correia
Algoritmi Research Center, Universidade do Minho, Campus de Azurém, 4800-058 Guimarães, Portugal

Dr. V. Correia
IB-S Institute of Science and Innovation for Sustainability, Universidade do Minho, 4710-057, Braga, Portugal

Dr. N. Peřinka and Prof. S. Lanceros-Méndez
BCMaterials, Basque Center for Materials, Applications and Nanostructures
UPV/EHU Science Park
48940 Leioa, Spain
Email: senentxu.lanceros@bcmaterials.net

Dr. C. M. Costa
Centro de Química, Universidade do Minho, 4710-057 Braga, Portugal

Prof. S. Lanceros-Méndez
IKERBASQUE, Basque Foundation for Science
Bilbao
48009, Spain

Keywords: printed electronics, printed battery, smart label, humidity sensor

Sensing smart labels are an essential component of the Internet of Things (IoT) in order to provide identification and data. However, the widespread use of these labels into functional devices requires easy integration and power supply. In this work, a smart label is presented with integrated humidity sensor and printed battery. The smart label is composed by detection, communication, control and energy subsystems. It is based on a screen printed RLC circuit and a printed humidity sensor with electrical linear response. The printed battery based on lithium iron phosphate as active cathode material was fabricated with 6 single cells connected in series, leading to approximately 100 $mAh.g^{-1}$.

The printed humidity sensor has a linear response with a sensitivity of 0.004/% RH.

It is thus demonstrated the development of fully-printed smart labels, improving integration into a variety of applications.

1. Introduction

Modern society is highly dependent on energy, mobility and interconnectivity, strongly based on the development of advanced high-performance materials, including smart and (multi)functional materials, that all together are giving rise to the Internet of Things (IoT) concept and related technologies [1]. The IoT concept is based on three main pillars: sensors, communications and processing of information [1b], being used in applications including health care, environmental monitoring, and industry 4.0, among others [2].

With the emergence of printing technologies applied to the field of materials, low-cost, flexible, easy-to-integrate sensors with tailored response are being developed [1a, 3]. The combination of printing techniques with new material with tailored electrical and magnetic properties results in printed electronics, allowing a new generation of smart sensors [1a, 4], radio-frequency identification (RFID) [5], photodetectors devices [6], transistors [7], and batteries [8], among others [9].

As an example, smart labels obtained by printing techniques are suitable solutions for low-cost devices with integrated electronic circuit for information processing [10], able to be incorporated in a variety of substrates, including flexible ones [11]. Different IoT applications take advantage of smart labels for object recognition and tracking which are composed by different sensors, including, temperature, pressure or humidity [4]. As an example, smart labels for food quality monitoring and security [12] based on printing technologies [13] allow time-temperature indicators (TTI) necessary in the food packaging industry [14].

Further, screen- printed RFIDs have been developed for smart food packaging with temperature, humidity and volatile amine compounds sensors, allowing to evaluate the freshness of the fish [15]. Similarly, a smart RFID label produced by inkjet-printing has been

presented for environmental monitoring. It allows measuring humidity, temperature and ammonia levels, based on capacity and resistive variations, respectively. The system is composed by a capacitive vapor detection (humidity), two channels for resistive based vapor detection (ammonia) with heating ability and a resistive channel for temperature detection (RTD) [16].

Further, a smart packaging system was presented, constituted by a wireless power transmission device, called rectenna (antenna, diode and capacitor), and humidity sensor was fabricated on poly(ethylene terephtalate) (PET) films while electrochromic signal units were manufactured by roll-to-roll (R2R) coating. The system was developed to detect food quality in packaging where the all-printed wireless-QR Code-humidity sensor tag displays the QR-Code just for a relative humidity above 70% [17].

For temperature sensing applications, smart label electronic systems using p-type organic thin film transistors (OTFT) were produced with approximately 180 p-type OTFTs operated with a V_{DD} of -20 V [18]. Taking into account environmental issues, smart labels for humidity measurements have been printed on recycled paper using paper as a dielectric material. The recycled paper-based sensors exhibit a signal variation of three orders of magnitude for relative humidity variations in the range 35% to 90% [19].

Independently of the detection system present in the smart label, the devices require a power source for the electronic circuit, typically based on a battery.

The interest on printed batteries is strongly increasing, considering their cost, security and simple integration into different substrates and applications [20].

Printed batteries are increasingly being studied based on different systems, including lithium-ion batteries [21] and Zn-MnO_2 [22], among others.

Printed interdigitated electrodes and polymer electrolytes for printed batteries [21] show that shorter Li^+ diffusion distances results in fast insertion kinetics of ions at increasing specific currents. Also, 3D printed Li-ion batteries based on $LiMn_{0.21}Fe_{0.79}PO_4$ nanocrystal cathodes

show long-term stability and high capacity in comparison to conventional batteries [23]. Important advances have been also performed in printable Li-ion battery electrolytes [20d, 24]. Thus, a solid-state printed battery was integrated with a pressure sensor and the corresponding a wireless communication system [25].

Taking into account the still limited state of the art with respect to smart labels, the present work focus on the fabrication and integration of an all-printed smart label powered by a printed battery for humidity sensing . The screen printed powered device is demonstrated based on an RLC circuit, paving the way for a new generation of integrated all-printed electronic sensing devices.

2. Results and discussion

2.1. Simulations, fabrication and characterization of the electronic components

Simulations were carried out for the design of the various subsystems that constitute the smart label.

2.1.1. Simulated and printed inductors

The implementation of a printed coil implies the definition of a large number of parameters. The simulation phase began with the evaluation, after equation 3 of the characteristics of the coil, L, Rs and Quality factor, as a function of number of turns (n) and line width (w), with the objective of obtaining a coil that maximizes the response of the sensor response.

The results of the simulation for the various parameters are presented in **Figure 1**.

Figure 1 a) shows a clear increase of the inductance L of the coil with increasing number of turns n. On the other hand, increasing number of turns implies smaller line width, since the area of implementation is fixed, and a larger total length of the printed line, leading to a strong increase of the resistance Rs (Figure 1b), in particular for coils with more than 10 turns.

On the other hand, it is observed that the quality factor Q is improved for larger line widths, the best response corresponding to a printed occupancy area of 60% to 66% (Figure 1c).

Further, by maintaining fixed the number of turns (n) and width of the line (w), it is shown that the square topology presents best results when compared with the circular one.

Thus, based on the results of Figure 1d) the optimized selected coil has the following characteristics: outer diameter of 31x31 mm, 10 turns with a line width of 700 μm corresponding to a total line length of ~ 0.66 m, leading to a relatively low Rs (19.5 Ω), an inductance of L ~ 2.47 μH and a suitable quality factor.

The coil equivalent circuit is shown in **Figure 2a)**, consisting in a series resistance (Rs), which corresponds to the resistance of the conductor, and a parallel capacitance, corresponding to the capacity formed by the several lines of the turns.

Only one layer is required to fabricate the coil, but to obtain the two coil terminals accessible to the rest of the circuit, it is necessary to add a bridge between the center of the coil and its outer pad, printing first a dielectric layer followed by the conductive layer.

After printing six replicates, the electrical tests were carried out to characterize the printed coils. According to the equivalent model, an inductance of 3.01 μH ± 8%, a serial resistance Rs of 41.8 Ω ± 8%, and a parallel capacitance Cp of 5 pF ± 10% was obtained (Figure 2b).

Comparing the simulations and the measurements of the printed coils, it is observed a 18% higher inductance value, which is attributed to the reduction of the space between the lines of the turns to 400 μm. It was also verified that the resistance of the printed coil is about 55% larger than the simulated value, which is related to irregularities in the obtained line, due to both the printing and curing process, given its total length of 0.66 m.

As for the quality factor there is a decrease when compared to the simulated value in the order of 42% and being this a planar coil, a capacity value is obtained in the order of 5 pF, however, this value will not have a large influence on the final response of the circuit.

2.1.2. Simulated and printed capacitors

The printed capacitor is a parallel plate capacitor composed by two conducting layers separated by a dielectric layer. The thickness of the dielectric layer and the dielectric properties of the ink are the two key factors that define the capacitance per unit area. Another important issue to take into consideration corresponds to the uniformity of the obtained layers, avoiding the formation of a short circuit between the conducting layers [26]. Square patterns were printed to form the first capacitor plane (**Figure 9**) with an active area of 5 x 5 mm^2.

After curing the silver ink layer (conditions indicated in Figure 9), the UV dielectric layer was printed, to guarantee a uniform layer and to prevent short circuit between the first and the third conductive layers. The size of this layer is 5.5 x 5.5 mm^2, ensuring the perfect isolation between layers.

After the UV curing of the dielectric layer, the capacitor is finished by printing a new silver conductive layer corresponding to the top conducting electrode. This layer is also subjected to a curing process, as indicated in Figure 9.

In agreement with the theoretical capacitor calculation, considering an estimated thickness of ~13 μm for the dielectric layer and an area of the conductive plates of 5.5 x 5.5 mm^2, a capacitance of 97.7pF would be obtained (**Figure 3a**).

After the printing of six capacitors, the electrical measurements (according to the equivalent model presented in Figure 3a) provided a capacitance of 96.5 pF ± 1% (Figure 3b), a serial resistance (Rs) of 2 Ω ± 5%, a parallel resistance (Rp) of 129 MΩ and a serial inductance (Ls) that is assumed to be 0 H, as the value is smaller than the minimum resolution of the equipment. Figure 3c) shows the cross-section SEM image obtained in the multilayer device. The sectional image shows the dielectric layer between the silver conductive layers with a homogeneous morphology.

Thus, the printed capacitor shows a perfect approximation between the calculated value and the measured one, provided that a uniform dielectric layer of the desired thickness is obtained.

2.1.3. Simulated and printed resistors

Based on equation 4 and the volume resistivity of the PEDOT ink (ρ = ~ 0.015 Ω.cm) it is just necessary to take into account geometrical considerations to obtain a specific resistance value. It was found that for the selected mesh and a thickness after curing of 3 μm, the L / W ratio must be 0.9 in order to obtain a resistance of 45 Ω. It is to notice that several layers can be also printed in order to increase the thickness of the resistance and therefore reduce the printed area to obtain a specific resistance value. Nevertheless, it is also important to consider that the increase in thickness may not be linear with the number of layers due to the effect of the solvent present in the printing of the upper layers on the layers already printed [26a].

2.2. Printed battery

The smart labels require a high voltage power source to operate. Thus, a high voltage battery has been developed by connecting low voltage single cells. More details about this full cell can be obtained in [27]. The full cell is composed by 6 single cells connected in series and integrated in the smart label. The battery was fabricated by screen-printing technique and the corresponding charge/discharge profiles are presented in **Figure 4a)** showing just the third curve. The charge/discharge profile is the typical of a battery based on graphite and LFP electrodes but six times higher than that of the single cell.

The morphology of the printed electrodes is shown as insert images in Figure 4b). Regardless of the electrode type (anode or cathode), there is a good distribution of active materials without large aggregates.

In order to evaluate the cycle stability, Figure 4b) shows the charge capacity value during 10 cycles, showing a good stability with high capacity retention over 10 cycles.

Considering the battery performance presented in Figure 4, it is a suitable power source for the RLC oscillator circuit, with easy integration in the smart label device.

2.3. Simulated and printed smart label

The RLC circuit was also simulated, based on the equivalent model presented in **Figure 8**.

The various layers of the complete circuit were designed according to the conditions necessary for manufacturing the various components previously described. The printed circuit is shown in **Figure 5a).** By analyzing the printed structures by profilometry in the regions indicated in Figure 5b) and Figure 5c), it is verified that the silver layer has a thickness around 5 μm and the dielectric layer has a thickness around 11 to 13 μm, depending on the measurement region, indicated in Figure 5a).

In this way it is possible to predict the response of the circuit when subjected to a variation of the sensor resistance of 1 Ω, 10 Ω, 100 Ω and 1 kΩ when a sufficiently long pulse is applied to charge the capacitor. In the simulation process, a 20V pulse is applied with a duration of 10 ms to the smart label circuit, the results of this simulations being shown in Figure 5 d).

Figure 5 d) shows that the variation of the attenuation time at the resonance frequency of the circuit is evidenced, when there is a variation in the sensor resistance. It is to notice that in an ideal circuit, if the resistance of the sensor is 0, the circuit will remain oscillating infinitely with a frequency defined by the value of C and L, according to equation 2.

Since it is not an ideal circuit, as indicated by the equivalent models of the various components, the circuit presents an attenuation of the response to sensor values close to zero, thus corresponding to the attenuation of the equivalent resistance of the non-ideal circuit, which is approximately 48 Ohms.

Thus, by the simulations it is expected to observe a variation in the sensor from 1 Ω to approximately 1 kΩ, measuring the damping time between 1 us and 0 respectively.

The functional tests of the circuit were carried out incorporating the printed battery and evaluating the impulse response of the circuit, on the side of the signal receiving platform coil (Figure 5e). The result of the response is present in the Figure 5e), without any filter or signal conditioning. For digital signal acquisition, a sampling rate of 400 MHz was used, which allows a future digital analysis of the signal according to the oscillation frequency of the circuit, which would allow to remove part of the present noise, evidencing with larger clarity the attenuation of the response. As shown in Figure 5e), the response of the circuit is very close to the simulated response. Therefore, it is possible to identify the variation of the sensor in the ranges defined by the attenuation of the oscillation and the oscillation frequency is situated around 5 MHz, even without signal treatment. Increasing the resolution of the system will require a digital filtering of the signal through a band pass filter centered at 5 MHz, thus reducing noise acquired during the communication process.

2.4. Humidity sensor characterization

The printed resistive humidity sensor is based on the variation of the resistance of the active PVA layer deposited on the interdigitated electrodes as a function of the ambient humidity, where the resistance R_0 can be defined by the geometric factor of the channel formed by the interdigitates. Ideally, the R_0 values should be 1 kΩ. Nevertheless, in the present case the R_0 value was optimized considering conductive patterns, as the selected geometry allows to optimize sensor response. Thus, the sensor is printed based on interdigitated conductors (**Figure 6a**)) with a line thickness of 300 μm with a finger spacing of 300 μm, with a total of 6 fingers in each contact. The sensor active layer is then printed on top, uniformly covering the entire surface of the sensor.

For the developed sensors, the multilayer structure was analyzed through SEM, the silver layer thickness being in agreement with the previously presented printed conductive patterns. The active layer thickness is approximately 3 μm (Figure 6b) with an average surface roughness

(Figure 6c) of 41 nm, as evaluated after AFM. This surface roughness corresponds to about 1.3% of the thickness of the layer and is a relevant factor for humidity absorption.

The relative response of the sensors for relative humidity variations in the range between 40% and 90% was obtained (Figure 6d). For the sensor with the 277 mm channel (30 fingers with area of 9.3 × 15 mm), it shows a ΔR for the defined humidity range of 632 Ω, thus, ΔR / R40% (relative resistance variation for the interval) is equal to 0.17. For the sensor with the 800 mm channel (40 fingers with area of 20 × 20 mm), ΔR for the humidity range is 289 Ω, i.e ΔR / R40% is equal to 0.20.

For each sensor, the sensitivity value was calculated using equation 1 [28]:

$$S = \left(\frac{1}{R_{Ti}}\right)\left(\frac{R_{Ti}-R_{Tf}}{RH_i-R_{Hf}}\right) \quad (1)$$

where R_{Ti} and R_{Tf} are the resistance values obtained at initial RHi and final humidity value RH_f.

The sensitivity value for the sensors with the 277 mm and 800 mm channels is 0.0034 and 0.004/% RH, respectively, being possible to conclude that the sensor with the largest channel presents a larger relative response in the defined interval as well as a better linear response, as observed in Figure 6d. Thus, a better linear response is associated with a larger variation in resistance for the interval, showing that the sensor with the largest channel is more suitable for this application. It is to notice that the sensitivity values reported in this work are similar to others reported in the literature for materials based on carbon nanotubes [28].

To assess the stability of the sensor with 800 mm channels, **Figure 7a)** shows the response of the resistance value to different humidity values as a function time.

Figure 7a) shows that the printed humidity sensor presents a very stable response as a function of time, as well as a suitable R_0 value for this system, since this R_0 value has implications for the sensor sensibility and response. Figure 7b) shows the humidity sensor response time, in which it can be observed that when the relative humidity is increased from 40% to about 90%,

the sensor presents a rapid and reproductive response time without hysteresis. In addition, this device shows a higher sensitivity compared to the literature for smart RFID labels with 3.44 ± 0.1 fF/ %R.H. at 40 °C and lifetime of 57 days [16] and 1.1 kHz per %RH for wireless humidity sensor labels manufactured using screen-printing and dry-phase patterning, which presents considerable hysteresis for rapid changes in relative humidity [29].

Therefore, these results show a functional smart label device fabricated by screen-printing, a highly reproducible manufacturing method with fabrication success rates above 99%. The smart level includes integrated battery and humidity sensor capabilities, suitable for flexible and lightweight applications.

3. Conclusion

This works presents an all screen-printed smart label based on an oscillating RLC circuit with humidity sensor. For all passive components, the materials and manufacturing steps, the component characteristics and the equivalent circuits are provided. This oscillating RLC circuit receives power from a printed battery developed based on PVDF-TrFE as separator and electrodes manufactured by screen-printing.

For the printed components, capacitors with a density of ~ 0.32 nF/cm^2, coils with an inductance of 3.0 μH for a 31 x 31 mm printed area and a resistance of 49 Ω for a L/W printed ratio of 0.9, are obtained.

With the obtained components, an RLC oscillator circuit was fabricated and tested, communicating to a signal reception platform, where the variations of the circuit response are obtained.

Further, a humidity sensor was integrated with excellent electrical response as a function of relative humidity variation and stability over time for constant relative humidity value.

In summary, it has been demonstrated the possibility of developing fully functional printed electronic circuits for smart label applications, with improved integration by the possibility of

being printed directly on the desired surfaces and suitable for applications in large and flexible areas.

4. Experimental Section

4.1. Circuit design and simulation

The design of the smart label requires the optimization of the different subsystems necessary for its implementation, the main ones being:

1) Detection subsystem: able to monitor the specific environmental parameters, being relative humidity in the present case.

2) Communications subsystem: allowing the exchange of information of the measured parameters.

3) Control subsystem: allowing defining the time at which the information is collected and transmitted to the management platform.

4) Energy subsystem: responsible for powering the various smart label subsystems.

5) Smart management subsystem: external to the smart label and responsible for the management of the received information.

Figure 8 shows a schematic representation of the different subsystems of the fully printed smart label, together with the equivalent model of the detection circuit.

The proposed system is based on an RLC oscillator circuit (Figure 8f) showing an amplitude attenuation of the oscillation frequency, according to the variation of the resistive sensor. A battery feeds the reading circuit whenever the operator presses the button for acquiring the sensor information, leaving the detection and communication circuit to oscillate until the energy from the pulse is dissipated by the resistive part of the circuit. For the fabrication of the detection circuit represented in Figure 8f), it is necessary to develop a set of printed electronic components, including resistances, capacitors and coils [26] with specific characteristics, taking

also into consideration the printing method, in this case screen printing, for the fabrication of the electric circuit.

Thus, to design the electronic system, it is first necessary to fix some parameters for proper circuit operation.

One of the main issues corresponds to the frequency of resonance of the circuit, which is intended to be in the order of 5 MHz, according to the optimum frequency of the selected receiving circuit.

For the oscillator circuit, the oscillation frequency is defined by:

$$f = \frac{1}{2\pi\sqrt{LC}} \tag{2}$$

where *C* is the capacitance and *L* is the inductance, corresponding to C_1 and L_1, respectively, in the schematic representation presented in Figure 8f).

It is to notice that the resistive part of the circuit does not influence its resonance frequency, being nevertheless responsible for attenuating the amplitude of the oscillation frequency over time. Thus, in the design of the circuit it is important to ensure that the resistive component is low.

Taking into account the equivalent circuit of Figure 8f), the inductive part of the circuit (coil) was set to cover an implementation area of 30 mm x 30 mm, varying the remaining parameters in a simulation, including number of turns, line thickness, series resistance and Quality factor. The variation of the inductance with the geometry (square or circular) was also simulated for a fixed number of turns and thickness of the printed line.

Simulations were carried out for a single layer planar spiral coil inductor [30], which is based on the following equation for the inductance [31]:

$$L_{gmd} = \frac{\mu n^2 d_{avg} c_1}{2}\left(ln\left({}^{c_2}/_{\rho}\right) + c_3\rho + c_4\rho^2\right) \tag{3}$$

where μ is the vacuum permeability, n is the number of turns, ρ is the fill ratio, $d_{avg}$is the average diameter and the coefficients $c_i, i = 1, 2, 3, 4$ are layout dependent. More details on the layout dependence can be found in [31].

The resistive component of the printed coil must be taken into account in the design of the RLC circuit, since it can overshadow the resistance variation of the resistive sensor. The resistive component of the designed coil was simulated through:

$$R = \rho \frac{L}{T.W}[1 + \alpha(temp - 25)] \quad (4)$$

where the ρ is material resistivity, *W* is the width of the printed line, *L* is the length and *T* is the height and α is the temperature coefficient of resistance of the material. For the simulations, it was considered an ink resistivity of 10^{-6} Ω.cm, and a line thickness of 5.5 μm.

The capacitive component of the printed circuit is a parallel plate capacitor [26a], calculated after:

$$C = \frac{\varepsilon A}{d} \quad (5)$$

where ε is the dielectric permittivity of dielectric layer, *A* the area of the conductor plate and d the distance between the parallel plates

It is important to note that the uniformity of the layer and the material used in the dielectric layer are key issues to obtain good results in the fabrication of printed capacitors.

For the purposes of circuit design (Figure 8f), the simulation results were based in the best inductance (quality factor) options, in the capacity value calculated according to the resonant frequency to be obtained, and applying a variation of the simulated resistive sensor, observing the attenuation of the resonance frequency over time. The circuit simulation program was Multisim from National Instruments for analog electronic circuits, allowing to obtain the most appropriate design for the printed circuit of the smart label, ensuring the desired oscillation frequency and maximizing the response to the variation of the sensor resistance.

4.2. Materials and fabrication process of the smart label

4.2.1. Materials

Polyethylene naphthalate (PEN) films (Dupont Teijin Q65FA) with a thickness of 125 μm were used as flexible polymer substrates, according to the curing temperatures required in the manufacturing process.

Conductive silver nanoparticle ink Metalon® HPS-021LV from Novacentrix was used for the manufacture of the electrodes. This ink is characterized by a low curing temperature and a resistance of ~ 10 mΩ / sqr. Previous to the printing process, the ink was agitated by magnetic stirring in order to homogenize the dispersion and to obtain a viscosity in the order of 32 Pa.s.

For the dielectric layers, the 118-12A/B119-44 solvent-resistant ink from Creative Materials (USA) was used.

The resistive layer was fabricated from a PEDOT ink Orgacon™ EL-P-5015, (PEDOT:PSS, Poly(2,3-dihydrothieno-1,4-dioxin)-poly(styrenesulfonate)) from Sigma-Aldrich.

The sensor implemented in the circuit corresponds to a relative humidity sensor and was fabricated based on PEDOT:PSS–PVA as active material [32].

4.2.2. Fabrication process of printed circuit

The several layers needed to fabricate the electronic circuit by screen printing were designed through a vector drawing software and are represented in **Figure 9**. The first layer corresponds to the main conductive pattern, the most complex layer of higher definition, thus avoiding possible errors in subsequent printed layers and allowing to detect early stage faults.

The printing of the different layers was carried out by screen printing, using a semi-automatic printing equipment, model DX-3050D from DSTAR, with a vacuum table and adjustable speed

for the printing squeegee rulers. For the printing of the patterns of the different layers, a stencil with 550 × 450 mm frame dimensions placed at 3 mm distance of the substrate and a printing velocity of 0.3m/s were used. The characteristics of the mesh are dependent of the used inks. Thus, for the conductive ink a polyester screen with mesh size of 264 × 264 threads per square inch, with gaps of 55 μm and a mesh tension of 20 N was used. The dielectric layer requires a polyester screen with mesh size of 264 × 264 threads per square inch, with gaps of 55 μm and a mesh tension of 20 N. For the PEDOT-based ink, the same mesh was used.

In turn, due to the characteristics of the PVA/PEDOT ink, a polyester screen with mesh size of 158 × 158 threads per square inch with gaps of 64 μm and a mesh tension of 20 N was used.

Before printing, the PEN substrates were cleaned with ethanol and dried with nitrogen to remove any remaining particles. For the deposition of the bottom structure, the silver ink was printed using a printing speed of 1 m/s, and then cured at temperatures of 120 ° C for 30 min, through an electric Convection Forced Oven (JP selecta 2005165). The same process was repeated for the remaining layers, according to the curing characteristics presented in Figure 9. The smart label has been reproduced ten times and the presented results are representative for all devices.

4.2.3. Characterization of the printed layers

Scanning electron microscopy (SEM) images were obtained with a Zeiss Auriga microscope.

The layer thickness was measured by profilometry (Veeco Dektak 150), each measurement being performed in triplicate.

The surface topography of the printed layers was evaluated by atomic force microscopy (AFM) in the tapping mode with a NTEGRA Aura (NT-MDT, Russia) set up with NSG01 non-coated silicon probes with 1–5 N/m spring constant.

The electrical characterization of the different printed electronic components was carried out in the 20 Hz to 1 MHz frequency range using a QuadTech 1920 Precision LCR Meter connected

to the control computer via IEEE-488 interface. The connection between the LCR meter and the specific component to be characterised was performed making use of ball point needles coated with gold. The following parameters were obtained: series inductance (L) and series resistance (Rs) for the coils; parallel capacitance (C) and parallel resistance (Rp) for the capacitors; and resistance (R) for the resistances.

Further, the complete circuit was characterized by evaluating its response to resistance variation. In order to guarantee stability during the characterization process, the sensor was replaced by a standard resistance set in the range from 1 to 1000 Ohms, recording the oscillating response of the circuit, through a 25 MHz digital oscilloscope (PicoScope, model 2205A).

For the evaluation of the relative humidity variations, a setup was built using an airtight vapor chamber (P-Selecta) with temperature control in which the environmental humidity was created with an ultrasonic humidifier in a 100 mL beaker with distilled water at 24 ºC. The variation of resistance was obtained for the humidity variation from 40% to 90%, where the printed sensor resistance was measured using a HP 34401 digital multimeter connected to a PC for data acquisition.

4.3. Printed battery

4.3.1. Preparation of electrode inks

The materials used for the development of the electrode inks were: Graphite (Timcal Graphite & Carbon) or C-$LiFePO_4$ (LFP, Phostech Lithium), carbon black (Super P, Timcal Graphite & Carbon, Switzerland) and poly(vinylidene fluoride), PVDF, (Solef 5130, Solvay) as active material for anode or cathode, conductive additive and polymer binder, respectively. The materials were mixed in a weight ratio (%) of 80:10:10 for active material, conductive additive and polymer binder, respectively. First, the polymer binder was dissolved in methylpyrrolidinone (NMP, Fluka) to form the polymer binder solution (40 mg/mL), and then

the active material and conductive additive were added to the solution. More details on the electrode preparation are reported in [27]. The resulting slurry for anode and cathode electrodes was then casted on copper and aluminum foils, respectively by screen-printing technique and dried at 80ºC for 2 h. The active mass loading for anode and cathode was ~ 1.8 and 0.8 $mg.cm^{-2}$, respectively.

4.3.2. Printed battery fabrication and characterization

The LIBs were fabricated using Al pouch cells with 6 cells connected in series in which the unit cell has a voltage of 3.4 V. The fabrication took place in an argon-filled glove box in which the prelithiation of the graphite electrode was also carried out. Graphite electrode on Cu foil was used as anode, the C-$LiFePO_4$ electrode on aluminium as cathode and PVDF-TrFE polymer as separator soaked in 1M $LiPF_6$ in ethylene carbonate-diethyl carbonate (EC-DEC, 1:1 vol) solution. Details about the separator preparation are provided in [33]. The average capacity ratio (N/P), Negative (N, graphite, 350 $mAh.g^{-1}$)/Positive (P, LFP, 140 $mAh.g^{-1}$) ratio is 0.924. Charge-discharge tests were obtained at room temperature using a Biologic VMP3 instrument.

Acknowledgements
The authors thank the FCT (Fundação para a Ciência e Tecnologia) for financial support under the framework of Strategic Funding grants UID/FIS/04650/2020, UID/EEA/04436/2020 and UID/QUI/0686/2020 and project no. PTDC/FIS-MAC/28157/2017. The authors also thank the FCT for financial support under grants SFRH/BD/131729/2017 (N.P.) and SFRH/BPD/112547/2015 (C.M.C.). Financial support from the Basque Government under the ELKARTEK, HAZITEK and PIBA (PIBA-2018-06) programs is also acknowledged.

Received: ((will be filled in by the editorial staff))
Revised: ((will be filled in by the editorial staff))
Published online: ((will be filled in by the editorial staff))

References

[1] a) J. Oliveira, V. Correia, H. Castro, P. Martins, S. Lanceros-Mendez, *Additive Manufacturing* **2018**, 21, 269; b) L. Atzori, A. Iera, G. Morabito, *Computer Networks* **2010**, 54, 2787.

[2] a) J. Gubbi, R. Buyya, S. Marusic, M. Palaniswami, *Future Generation Computer Systems* **2013**, 29, 1645; b) D. Miorandi, S. Sicari, F. De Pellegrini, I. Chlamtac, *Ad Hoc Networks* **2012**, 10, 1497.

[3] a) A. McEwen, H. Cassimally, *Designing the Internet of Things*, Wiley, **2013**; b) J. Hast, S. Ihme, J. Mäkinen, K. Keränen, M. Tuomikoski, K. Rönkä, H. Kopola, presented at 2014 44th European Solid State Device Research Conference (ESSDERC), 22-26 Sept. 2014, **2014**.

[4] D. Briand, F. Molina-Lopez, A. V. Quintero, G. Mattana, N. F. d. Rooij, presented at 10th IEEE International NEWCAS Conference, 17-20 June 2012, **2012**.

[5] S. Kim, A. Georgiadis, M. M. Tentzeris, *Sensors* **2018**, 18, 1958.

[6] J. Oliveira, V. Correia, E. Sowade, I. Etxebarria, R. D. Rodriguez, K. Y. Mitra, R. R. Baumann, S. Lanceros-Mendez, *ACS Applied Materials & Interfaces* **2018**, 10, 12904.

[7] H. F. Castro, E. Sowade, J. G. Rocha, P. Alpuim, S. Lanceros-Méndez, R. R. Baumann, *Journal of Electronic Materials* **2014**, 43, 2631.

[8] A. Willert, C. Meuser, R. R. Baumann, *Japanese Journal of Applied Physics* **2018**, 57, 05GB02.

[9] a) Y. Zhan, Y. Mei, L. Zheng, *Journal of Materials Chemistry C* **2014**, 2, 1220; b) M. M, x00E, ntysalo, L. Xie, F. Jonsson, Y. Feng, A. L. Cabezas, L. Zheng, presented at 2012 IEEE 62nd Electronic Components and Technology Conference, 29 May-1 June

2012, **2012**; c) L. Roselli, C. Mariotti, P. Mezzanotte, F. Alimenti, G. Orecchini, M. Virili, N. B. Carvalho, presented at 2015 IEEE Topical Conference on Wireless Sensors and Sensor Networks (WiSNet), 25-28 Jan. 2015, **2015**.

[10] R. A. Street, T. N. Ng, D. E. Schwartz, G. L. Whiting, J. P. Lu, R. D. Bringans, J. Veres, *Proceedings of the IEEE* **2015**, 103, 607.

[11] Z. Li-Rong, M. B. Nejad, S. Rodriguez, Z. Lu, C. Cairong, H. Tenhunen, presented at Conference on High Density Microsystem Design and Packaging and Component Failure Analysis, 2006. HDP'06., 27-28 June 2006, **2006**.

[12] B. Kuswandi, Y. Wicaksono, Jayus, A. Abdullah, L. Y. Heng, M. Ahmad, *Sensing and Instrumentation for Food Quality and Safety* **2011**, 5, 137.

[13] E. Abad, F. Palacio, M. Nuin, A. G. d. Zárate, A. Juarros, J. M. Gómez, S. Marco, *Journal of Food Engineering* **2009**, 93, 394.

[14] S. Zabala, J. Castán, C. Martínez, *Food Control* **2015**, 50, 57.

[15] E. Smits, J. Schram, M. Nagelkerke, R. H. L. Kusters, G. Heck, V. Van Acht, M. Koetse, J. Brand, G. Gelinck, H. Schoo, *Development of printed RFID sensor tags for smart food packaging*, **2012**.

[16] A. V. Quintero, F. Molina-Lopez, E. C. P. Smits, E. Danesh, J. van den Brand, K. Persaud, A. Oprea, N. Barsan, U. Weimar, N. F. de Rooij, D. Briand, *Flexible and Printed Electronics* **2016**, 1, 025003.

[17] H. Kang, H. Park, Y. Park, M. Jung, B. C. Kim, G. Wallace, G. Cho, *Scientific Reports* **2014**, 4, 5387.

[18] R. Ganesan, J. Krumm, S. Pankalla, K. Ludwig, M. Glesner, presented at 2013 Proceedings of the ESSCIRC (ESSCIRC), 16-20 Sept. 2013, **2013**.

[19] M. Mraović, T. Muck, M. Pivar, J. Trontelj, A. Pleteršek, *Sensors* **2014**, 14, 13628.

[20] a) S. Lanceros-Méndez, C. M. Costa, *Printed Batteries: Materials, Technologies and Applications*, Wiley, **2018**; b) K.-H. Choi, D. B. Ahn, S.-Y. Lee, *ACS Energy Letters* **2018**, 3, 220; c) R. E. Sousa, C. M. Costa, S. Lanceros-Méndez, *ChemSusChem* **2015**, 8, 3539; d) C. M. Costa, R. Gonçalves, S. Lanceros-Méndez, *Energy Storage Materials* **2020**, 28, 216.

[21] K. Fu, Y. Wang, C. Yan, Y. Yao, Y. Chen, J. Dai, S. Lacey, Y. Wang, J. Wan, T. Li, Z. Wang, Y. Xu, L. Hu, *Advanced Materials* **2016**, 28, 2587.

[22] E. Madej, M. Espig, R. R. Baumann, W. Schuhmann, F. La Mantia, *Journal of Power Sources* **2014**, 261, 356.

[23] J. Hu, Y. Jiang, S. Cui, Y. Duan, T. Liu, H. Guo, L. Lin, Y. Lin, J. Zheng, K. Amine, F. Pan, *Advanced Energy Materials* **2016**, 6, 1600856.

[24] A. J. Blake, R. R. Kohlmeyer, J. O. Hardin, E. A. Carmona, B. Maruyama, J. D. Berrigan, H. Huang, M. F. Durstock, *Advanced Energy Materials* **2017**, 7, 1602920.

[25] W. H. Cheong, B. Oh, S.-H. Kim, J. Jang, S. Ji, S. Lee, J. Cheon, S. Yoo, S.-Y. Lee, J.-U. Park, *Nano Energy* **2019**, 62, 230.

[26] a) V. Correia, K. Y. Mitra, H. Castro, J. G. Rocha, E. Sowade, R. R. Baumann, S. Lanceros-Mendez, *Journal of Manufacturing Processes* **2018**, 31, 364; b) H. F. Castro, V. Correia, E. Sowade, K. Y. Mitra, J. G. Rocha, R. R. Baumann, S. Lanceros-Méndez, *Organic Electronics* **2016**, 38, 205.

[27] A. Gören, J. Mendes, H. M. Rodrigues, R. E. Sousa, J. Oliveira, L. Hilliou, C. M. Costa, M. M. Silva, S. Lanceros-Méndez, *Journal of Power Sources* **2016**, 334, 65.

[28] V. S. Turkani, D. Maddipatla, B. B. Narakathu, T. S. Saeed, S. O. Obare, B. J. Bazuin, M. Z. Atashbar, *Nanoscale Advances* **2019**, 1, 2311.

[29] X. Wang, O. Larsson, D. Platt, S. Nordlinder, I. Engquist, M. Berggren, X. Crispin, *Sensors and Actuators B* **2012**, 166– 167, 556.

[30] Single layer Planar spiral coil inductor calculator, http://www.tesla-institute.com/!app/sim/slpscic.php, accessed.

[31] S. S. Mohan, M. d. M. Hershenson, S. P. Boyd, T. H. Lee, *IEEE Journal of Solid-State Circuits* **1999**, 34, 1419.

[32] K. H. Choi, M. Sajid, S. Aziz, B.-S. Yang, *Sensors and Actuators A: Physical* **2015**, 228, 40.

[33] C. M. Costa, J. L. Gomez Ribelles, S. Lanceros-Méndez, G. B. Appetecchi, B. Scrosati, *Journal of Power Sources* **2014**, 245, 779.

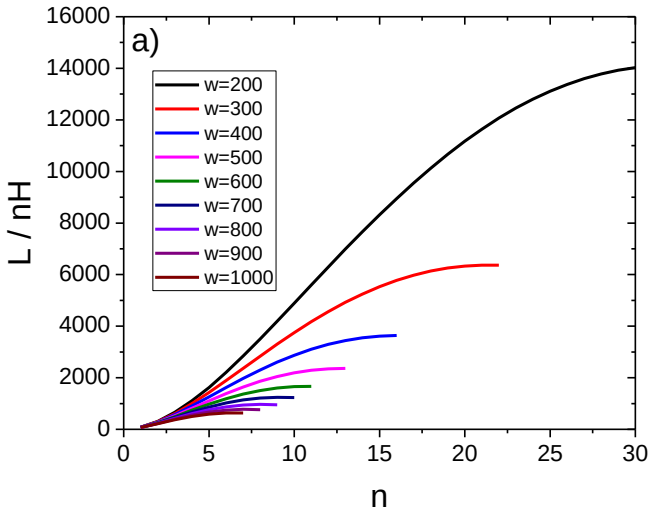

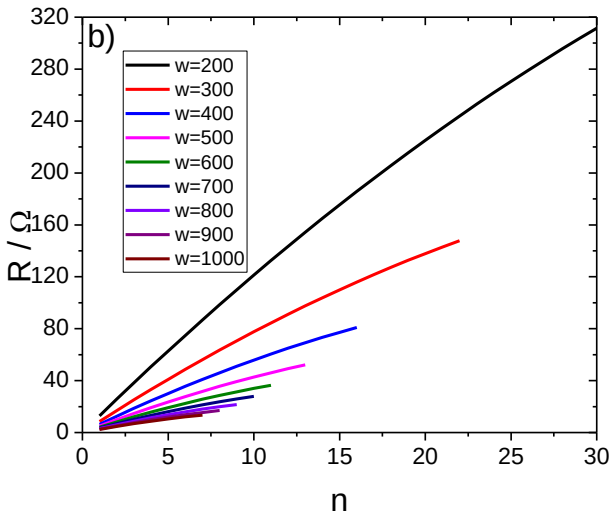

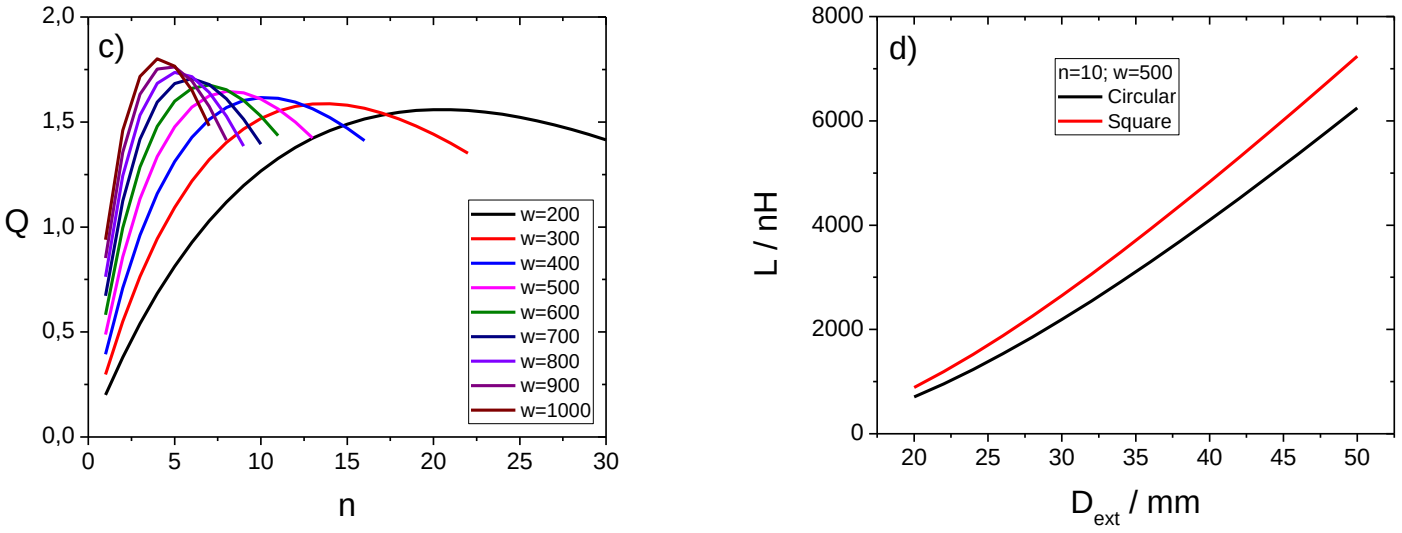

Figure 1. Simulation results for the printed coils: coil inductance (L) as function of number of turns (n) and line width (w) a); coil line resistance (Rs) as function of number of turns (n) and line width (w) b); coil quality factor (Q) as function of the number of turns (n) and line width (w) c); coil inductance L as function of external diameter (Dext) for 2 coil geometries d).

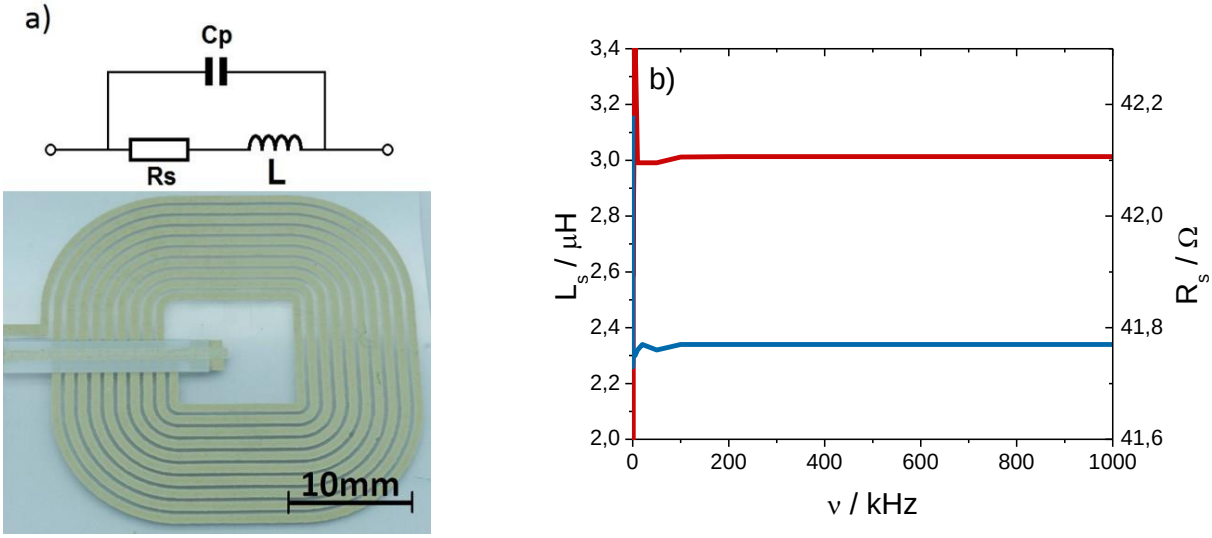

Figure 2. Printed planar coil equivalent circuit model with the printed coil image a) and inductance measurement as function of frequency b).

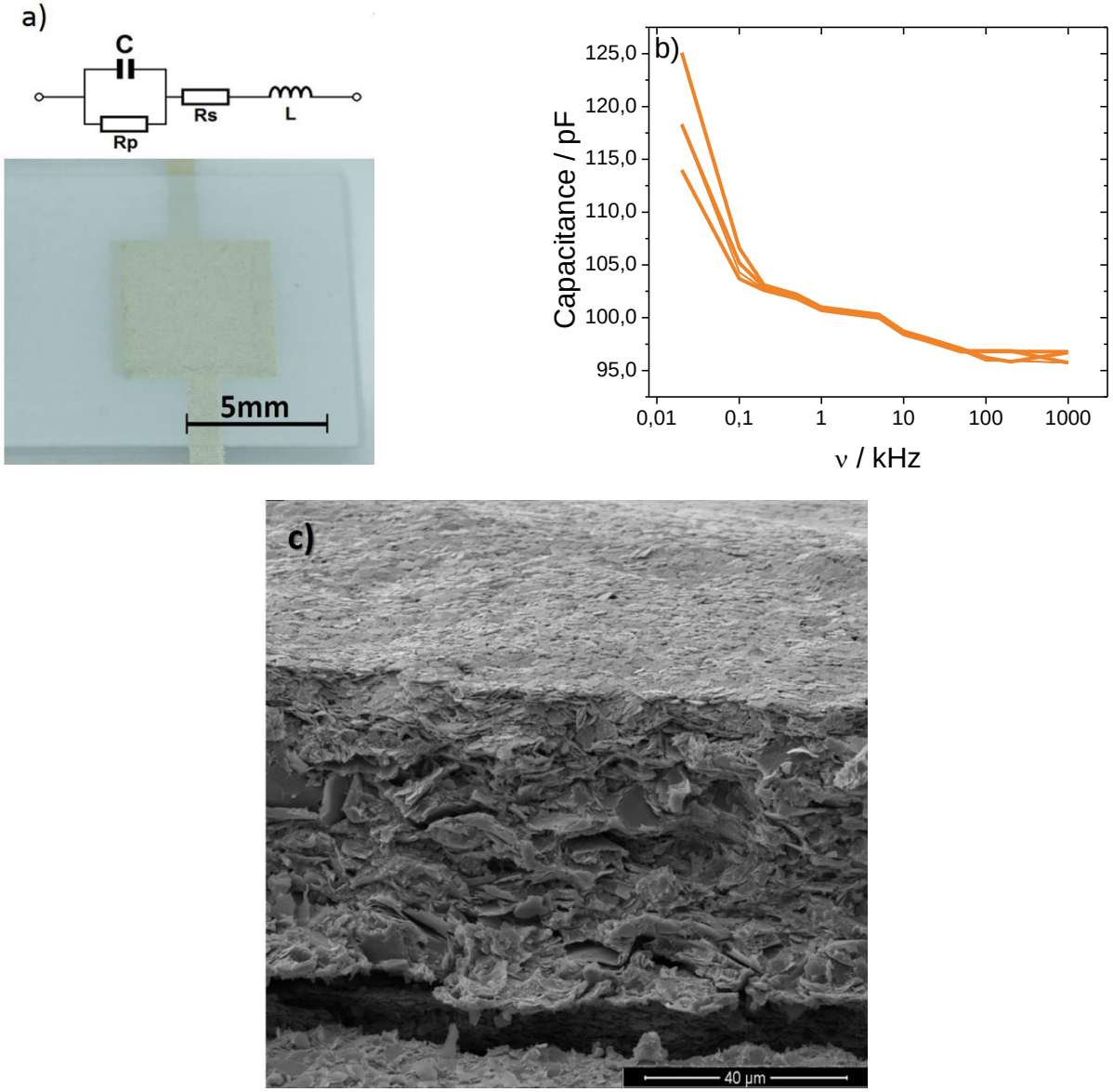

Figure 3. Printed planar capacitor equivalent circuit model with the image of a capacitor a), measured capacitance as a function of frequency b) and cross-sectional image of the capacitor c).

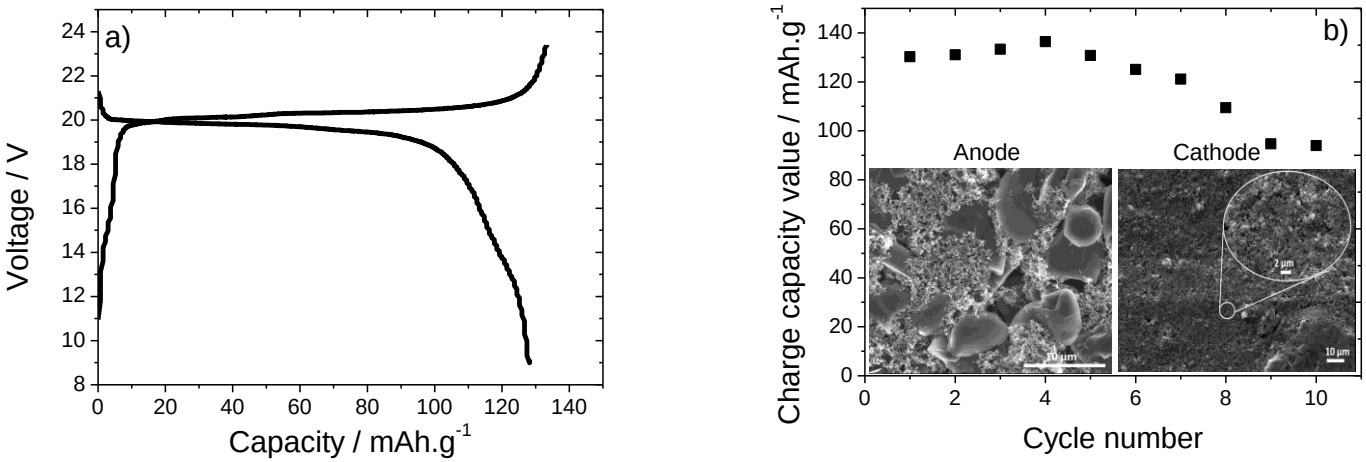

Figure 4. Room temperature charge and discharge profiles of the printed battery composed of single 6 cells (a) and charge capacity value when cycled for 10 cycles (b) (insert images: electrodes morphology images).

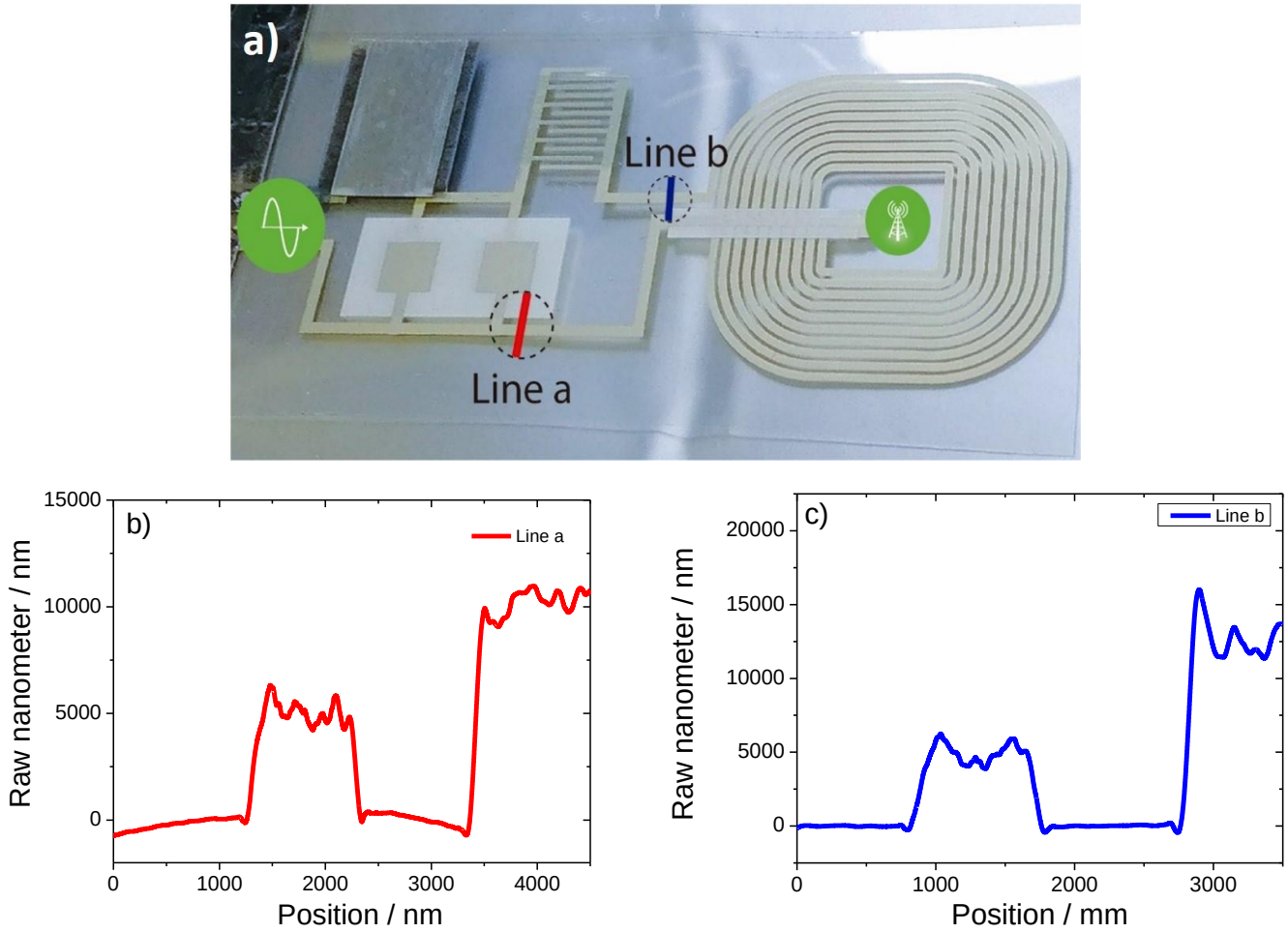

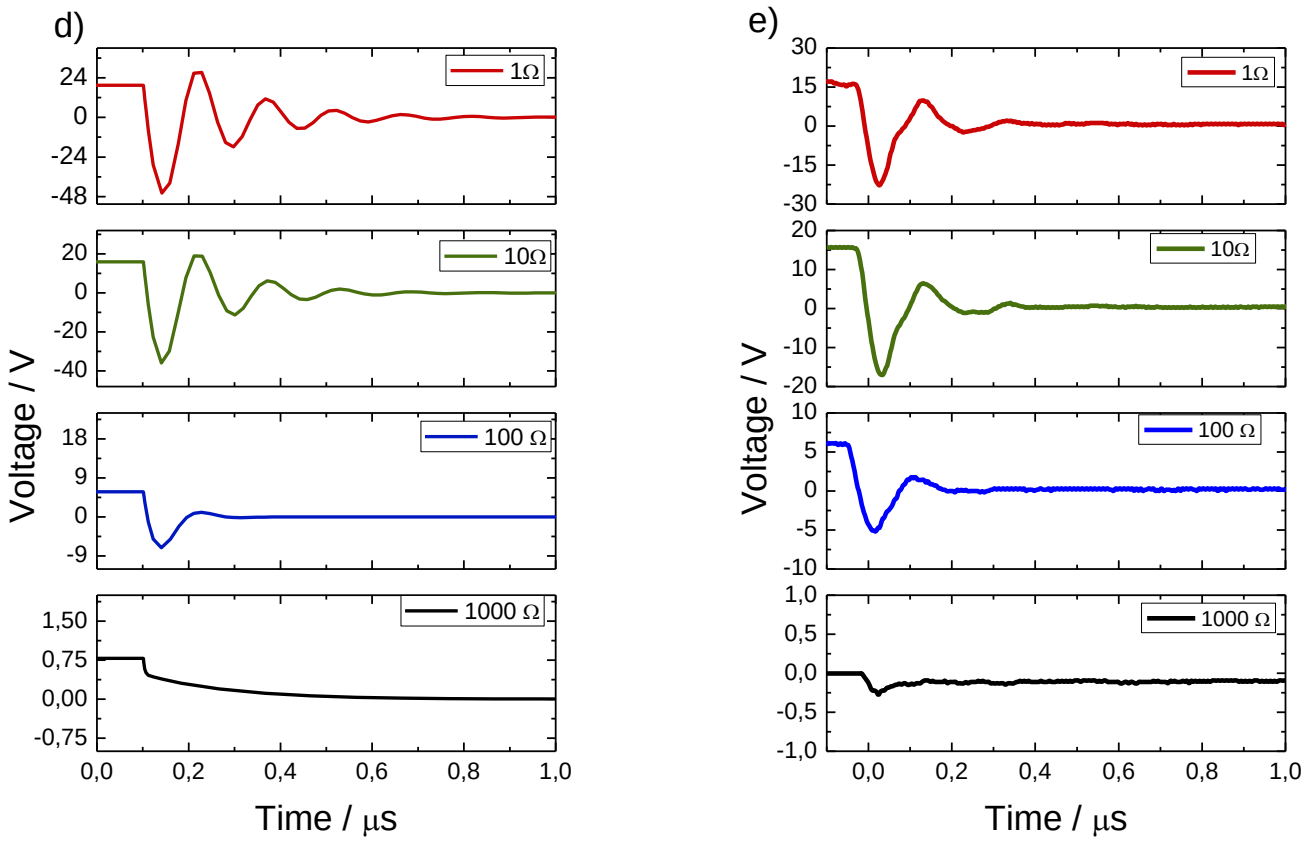

Figure 5. Printed RLC smart label circuit a); profilometry result at the regions indicated by line a (b) and b (c) of the final printed system b); simulations of the circuit response to an 20V impulse input for several resistance levels of the sensor d); circuit impulse actual response for several resistance levels of the sensor e).

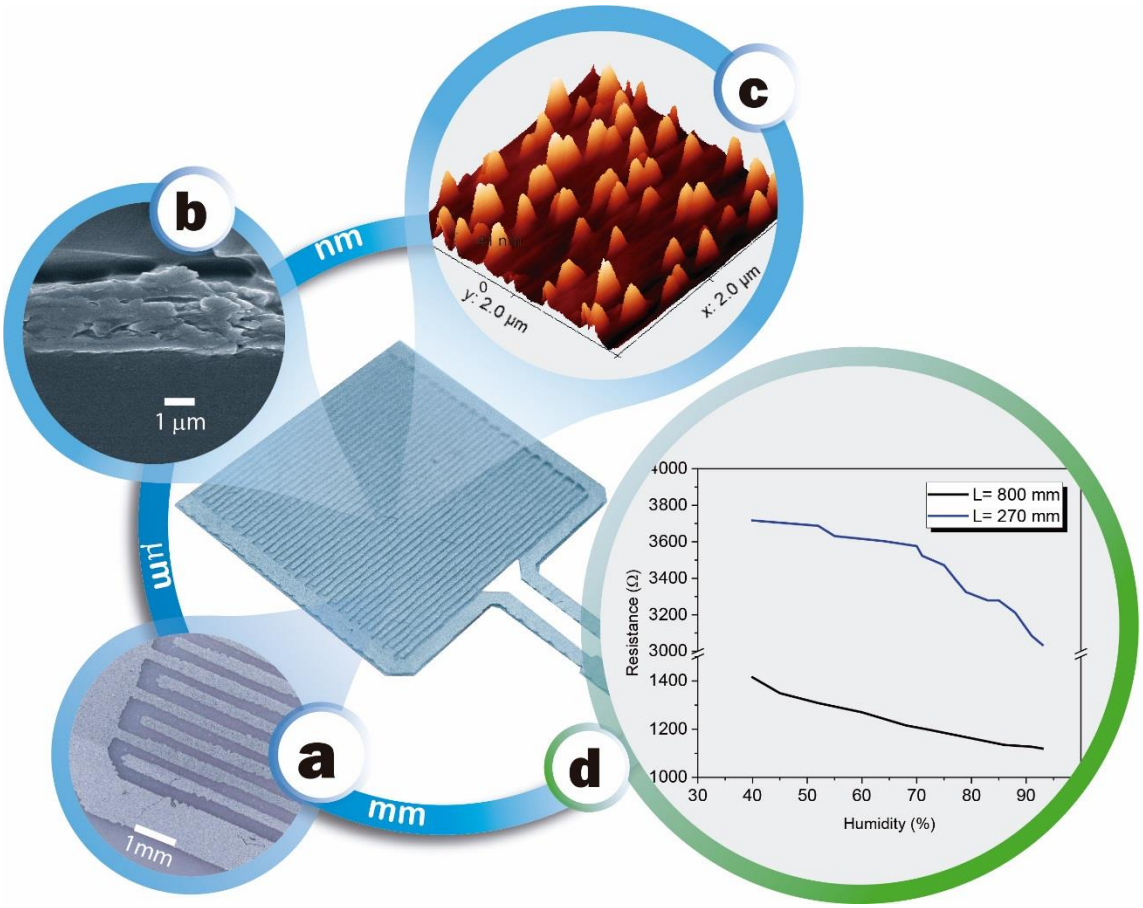

Figure 6. Picture of the printed humidity sensor. Detail of the interdigitated measuring channel a), cross section SEM image of the various layers, including the PVA active one b), AFM image showing the surface roughness of the PVA layer c) and electrical sensor response to humidity variations for two channel length densities d).

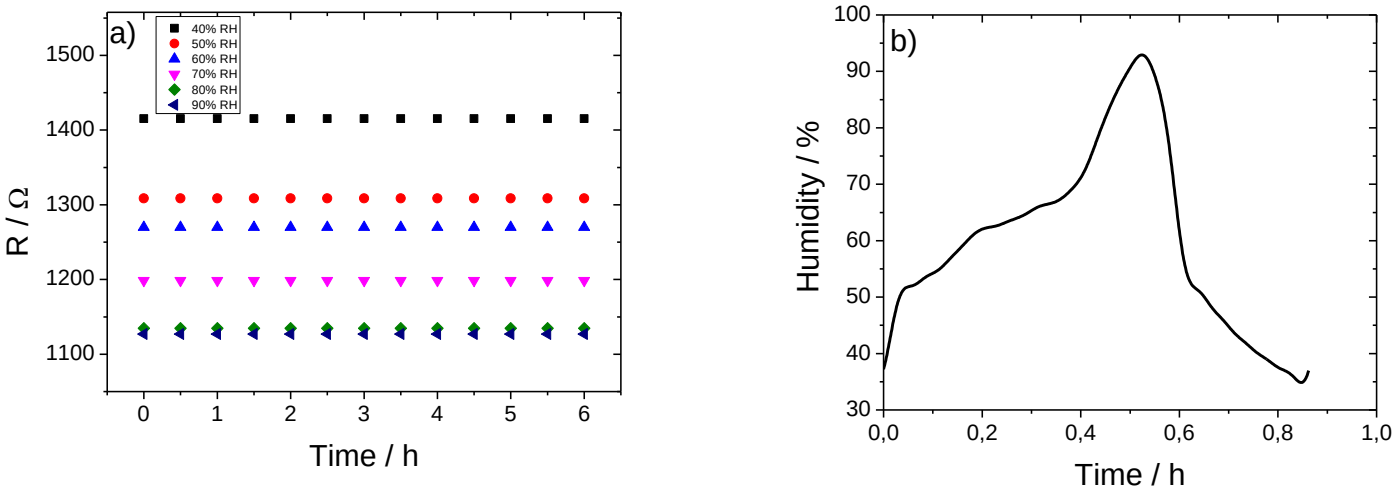

Figure 7. a) Time stability of the printed humidity sensor and b) sensor response to humidity tests.

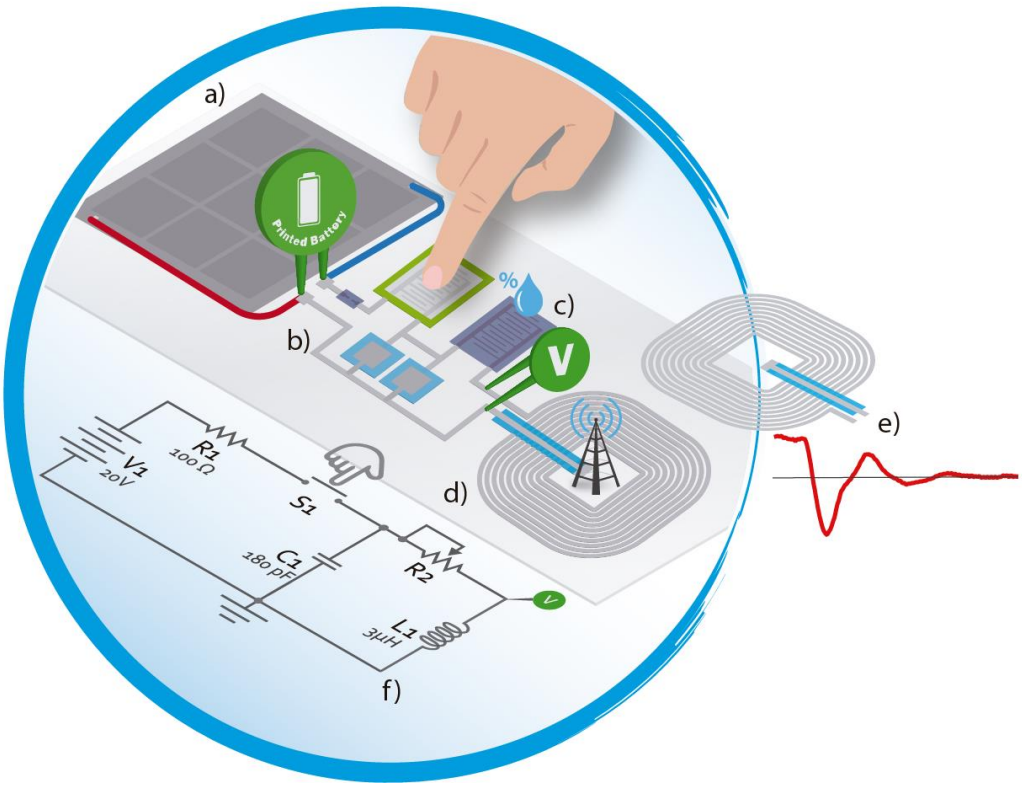

Figure 8. Schematic representation of the proposed all-printed smart label, in which the various subsystems are represented: Energy subsystem a), control subsystem b), detection subsystem c), communications subsystem d), smart management subsystem e). The equivalent model of the detection circuit f) is also presented.

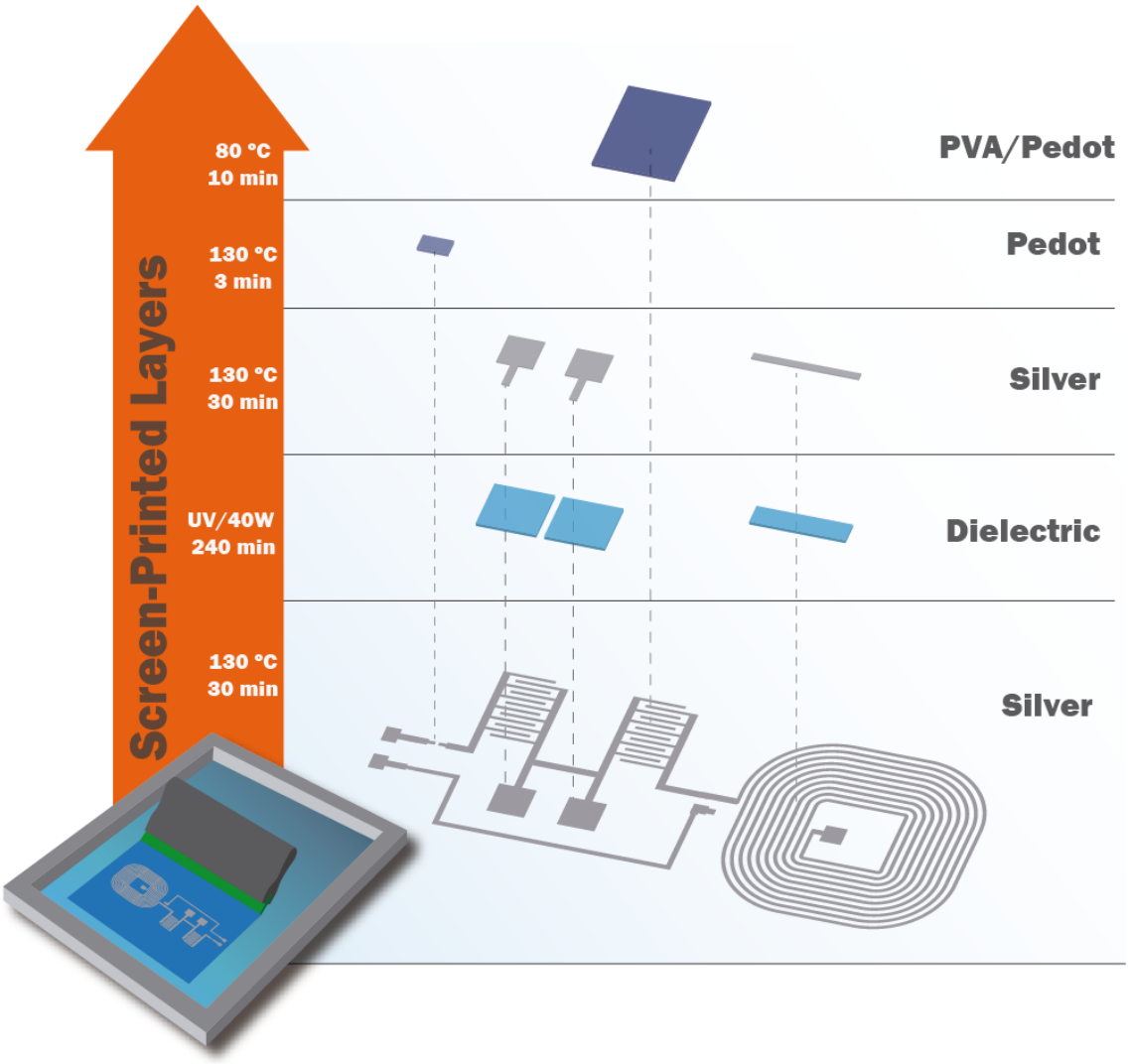

Figure 9. Schematic representation of the different printed layers and the corresponding printing sequence, from bottom to top. The curing conditions of the different layers are also indicated.

Functional labels require the integration of sensors and power supply. A smart label with integrated humidity sensor and battery is presented. The smart label has been fabricated by screen-printing and is composed by an RLC circuit. The printed humidity sensor shows a linear and stable response. Thus, it was demonstrated the possibility of developing all-printed electronic circuits with integrated sensing and power supply for smart label applications.

N. Pereira[1,2], V. Correia[2,3], N. Peřinka[4], C. M. Costa[1,5,*], S. Lanceros-Méndez[4,6,*]

All-printed smart label with integrated humidity sensors and power supply

ToC figure